JMR Journal of Meteorological Research

High Spatial Resolution and High Temporal Frequency (30–m/15–day) Fractional Vegetation Cover Estimation over China Using Multiple Remote Sensing Datasets: Method Development and Validation

Xihan MU, Tian ZHAO, Gaiyan RUAN, Jinling SONG, Jindi WANG, Guangjian YAN, Tim R. MCVICAR, Kai YAN, Zhan GAO, Yaokai LIU, Yuanyuan WANG

Citation: , 2020: High Spatial Resolution and High Temporal Frequency (30–m/15–day) Fractional Vegetation Cover Estimation over China Using Multiple Remote Sensing Datasets: Method Development and Validation. *J. Meteor. Res.*, **34**(6), 1–21, doi: 10.1007/s13351–021–0017–2

View online: http://jmr.cmsjournal.net/article/doi/10.1007/s13351–021–0017–2

High Spatial Resolution and High Temporal Frequency (30-m/15-day) Fractional Vegetation Cover Estimation over China Using Multiple Remote Sensing Datasets: Method Development and Validation

Xihan MU[1,2,3*], Tian ZHAO[1,2], Gaiyan RUAN[1,2], Jinling SONG[1,2], Jindi WANG[1,2], Guangjian YAN[1,2], Tim R. MCVICAR[3], Kai YAN[1,2,4], Zhan GAO[5], Yaokai LIU[6], and Yuanyuan WANG[7]

1 *State Key Laboratory of Remote Sensing Science*, *Faculty of Geographical Science*, *Beijing Normal University*, *Beijing* 100875, *China*
2 *Beijing Engineering Research Center for Global Land Remote Sensing Products*, *Faculty of Geographical Science*, *Beijing Normal University*, *Beijing* 100875, *China*
3 *CSIRO Land and Water*, *GPO Box* 1700, *Canberra*, *ACT* 2601, *Australia*
4 *Department of Earth and Environment*, *Boston University*, *Boston*, *MA*, *USA*
5 *Jiangsu Institute of Urban Planning and Design*, *Nanjing* 210036, *China*
6 *Aerospace Information Research Institute (AIR)*, *Chinese Academy of Sciences (CAS)*, *Beijing* 100094, *China*
7 *National Satellite Meteorological Center*, *China Meteorological Administration*, *Beijing* 100081, *China*

(Received February 17, 2020; in final form July 31, 2020)

ABSTRACT

High spatial resolution and high temporal frequency fractional vegetation cover (FVC) products have been increasingly in demand to monitor and research land surface processes. This paper develops the algorithm to estimate FVC at a 30-m/15-day resolution over China by taking advantage of the spatial and temporal information from different types of sensors: the 30-m resolution sensor on the Chinese environment satellite (HJ-1) and the 1-km Moderate Resolution Imaging Spectroradiometer (MODIS). The algorithm was implemented for each main vegetation class and each land cover type over China. First, the high spatial resolution and high temporal frequency normalized difference vegetation index (NDVI) was acquired using the continuous correction (CC) data assimilation method. Then, FVC was generated using a nonlinear pixel unmixing model. Model coefficients were obtained by statistical analysis of the MODIS NDVI. The proposed method was evaluated using *in situ* FVC measurements and a global FVC product (GEOV1 FVC). The direct validation using *in situ* measurements at 97 sampling plots per half month in 2010 showed that the annual mean errors (MEs) of forests, cropland, and grassland were −0.025, 0.133, and 0.160, respectively, and indicated that the FVCs derived from the proposed algorithm were consistent with ground measurements [R^2 = 0.809, root-mean-square deviation (RMSD) = 0.065]. The inter-comparison between the proposed FVC and GEOV1 FVC demonstrated that the two products had good spatial–temporal consistency and similar magnitude (RMSD approximates 0.1). Overall, the approach provides a new operational way to estimate high spatial resolution and high temporal frequency FVC from multiple remote sensing datasets.

Key words: fractional vegetation cover (FVC), high spatial resolution and high temporal frequency, data fusion, normalized difference vegetation index (NDVI), pixel unmixing model, multiple remote sensing datasets

Citation: Mu, X. H., T. Zhao, G. Y. Ruan, et al., 2020: High spatial resolution and high temporal frequency (30-m/15-day) fractional vegetation cover estimation over China using multiple remote sensing datasets: Method development and validation. *J. Meteor. Res.*, **34**(6), 1–21, doi: 10.1007/s13351-021-0017-2.

1. Introduction

Fractional vegetation cover (FVC) is defined as the ratio of the vertical projected area of vegetation to the whole area (Yan et al., 2012). In terms of remote sensing techniques, it is most often the ratio of the green vegetation area in a grid cell to the entire pixel area (Lu et al., 2003; Donohue et al., 2009), though recent attempts in-

Supported by the National Key Research and Development Program of China (2018YFC1506501, 2018YFA0605503, and 2016YFB0501502), the Special Program of Gaofen (04-Y30B01-9001-18/20-3-1), and National Natural Science Foundation of China (41871230 and 41871231).

*Corresponding author: muxihan@bnu.edu.cn.

clude the non-photosynthetic component as well (Guerschman et al., 2015), and occasionally defined in the view direction (Purevdorj et al., 1998; Obata et al., 2012). The FVC is sensitive to the vegetation amount and can characterize the surface vegetation status in a horizontal perspective (Gutman and Ignatov, 1998). Additionally, it provides an alternative to the vegetation index for distinguishing the contributions of the soil and the vegetation canopy (Xiao and Moody, 2005; Verger et al., 2015).

Remote sensing is the only practicable way to generate FVC products at regional or global scales on account of its quick and large-scale data acquisition ability (Liang et al., 2013). There are three main methods for estimating FVC using remote sensing data (Xiao and Moody, 2005; Jiapaer et al., 2011; Yan et al., 2012; Jia et al., 2015) including: (i) empirical models, (ii) pixel unmixing models, and (iii) physical models. Among these methods, the pixel unmixing model estimates FVC at a subpixel level by decomposing a pixel into at least two portions: (a) green vegetation and (b) non-green background. Linear unmixing modelling assumes that the spectral reflectance or spectral vegetation index (VI) of a pixel is the linearly weighted combination of those two components (Zeng et al., 2000; Yan et al., 2012; Jia et al., 2015). The VI-based mixture model is the most widely used linear unmixing model in high resolution FVC estimation due to its simple model form and computational efficiency when processing large datasets (Gutman and Ignatov, 1998; Zeng et al., 2000; Lu et al., 2003; Montandon and Small, 2008; Wu et al., 2014).

Considerable progress has been made in the generation of FVC products with remote sensing techniques over regional and global scales (Table 1). However, three main issues limiting the widespread use of these products for practical applications remain. First, some products only contain limited land cover types (DeFries et al., 1999; Guan et al., 2012; Sexton et al., 2013; Broxton et al., 2014). Second, some products suffer from a relatively low spatial and/or temporal resolution (Gutman and Ignatov, 1998; Zeng et al., 2000). The operational FVC products, such as the Carbon Cycle and Change in Land Observational Products from an Ensemble of Satellites (CYCLOPES; Baret et al., 2007), GEOLAND2 (Baret et al., 2013), and Polarization and Directionality of the Earth's Reflectances (POLDER; Roujean and Lacaze, 2002; Lacaze et al., 2003), derived from Systeme Probatoire d'Observation de la Terre (SPOT)-VEGETATION and Advanced Earth Observation Satellite (ADEOS)-POLDER data, provided FVCs with global coverage at 10-day and 1–6-km resolutions. Third, efforts have been made to improve the temporal continuity in FVC estimation over large scale (Wu et al., 2014; Ding et al., 2015; Jia et al., 2015; Verger et al., 2015). However, the spatial resolution still requires substantial improvements to meet many operational requirements. Using the low resolution (herein 1 km) FVC might introduce a maximum error of about 0.35 due to the scale effect in heterogeneous regions (Zhang et al., 2006). For numerous applications, such as monitoring the dynamics of impervious surface area (Zhang et al., 2013), quantitatively analyzing the process of urban expansion and its impacts (Zhang et al., 2015), monitoring the change of urban greenness (Gan et al., 2014), and land management (Naqvi et al., 2013; Pan and Wen, 2014), FVC products with a spatial resolution of 30 m, or better, are needed. Table 1 lists the existing regional or global FVC datasets; note that there is no FVC product at high spatial resolution (herein defined as 30 m) and high temporal frequency (herein defined as once every 15 days). Filling this niche provides the motivation for this study.

High spatial resolution and temporally dense series of remotely sensed data are difficult to obtain because of the long revisit cycles of the satellites, frequent cloud contamination, and other poor atmospheric conditions (Price, 1992; Gao et al., 2006; Zhu et al., 2010; Emelyanova et al., 2013). Many algorithms have been proposed to simultaneously enhance resolution in space and time by combining high spatial resolution images with high temporal frequency data. A spatial and temporal adaptive reflectance fusion model (STARFM; Gao et al., 2006) and its enhancement (ESTARFM; Zhu et al., 2010) are the most widely-used data fusion algorithms for simulating daily Landsat-like surface reflectance (Emelyanova et al., 2013). However, these methods suffer from expensive computation and low accuracies in certain situations (Jarihani et al., 2014). Because of these reasons, the fusion methods of normalized difference vegetation index (NDVI) series were introduced in temporal–spatial fusion to generate high spatial resolution NDVI time series (Busetto et al., 2008; Cai et al., 2011; Li et al., 2014).

This paper aims to provide a practical approach to retrieve high spatial resolution and high temporal frequency FVC over a large scale using multiple remote sensing datasets. The continuous correction (CC; Cai et al., 2011) model is used to blend the high and low resolution NDVI data and to generate the basic data for FVC estimation. Then, the FVC product was generated using a nonlinear pixel unmixing model by applying the NDVI to FVC transformation coefficients. This paper is organized as follows. Section 2 provides a general description of the study area and datasets. Section 3 details the ap-

Table 1. Brief summary of the primary existing global or regional FVC datasets. Studies are ordered chronologically and then alphabetically

Study	Sensor	Spatial resolution/Temporal frequency	Area	Period	Algorithm	Definition
1–Gutman and Ignatov, 1998	AVHRR	0.15°, 30 days	Global	1985–1990	Pixel unmixing model	Fraction of green vegetation cover
2–Zeng et al., 2000	AVHRR	1 km, 30 days	Global	1992–1993	Pixel unmixing model	Fraction of green vegetation cover
3–Lacaze et al., 2003; Roujean and Lacaze, 2002	POLDER	6 km, 10 days	Global	1996–1997, 2003	Neural network	Fraction of green vegetation cover
4–García-Haro et al., 2005; García-Haro et al., 2005	SEVIRI	3 km, 1 day	Europe, Northern Africa, Southern Africa, and South America	2005–current	A statistical approach	Fraction of green vegetation cover
5–Bacour et al., 2006	MERIS	0.3 km, 30 days/ 10 days	Europe	2002–2012	Neural network	Fraction of green vegetation cover
6–Baret et al., 2007	SPOT-VEGETATION	1 km, 10 days	Global	1999–2007	Neural network	Fraction of green vegetation cover
7–Guan et al., 2012	AVHRR GIMMS, QuikSCAT SIR, AMSR-E, TRMM	10 km, 15 days	Southeastern Africa	1999–2008	Mean-Sensitivity Unmixing Algorithm (MSUA)	Fractions of tree, grass, and bare soil
8–Baret et al., 2013	SPOT-VEGETATION	1/112°, 10 days	Global	1998–current	Neural network	Fraction of green vegetation cover
9–Sexton et al., 2013	MODIS, Landsat	30 m, yearly	Global	2000, 2005	Linear regression	Vegetation Continuous Fields of tree cover (percent tree cover)
10–Wu et al., 2014	AVHRR, GIMMS, MODIS	10 km, 30 days	Global	1982–2011	Pixel unmixing model	Fraction of green vegetation cover
11–Jia et al., 2015	MODIS, Landsat (TM, ETM+)	0.5 km, 8 days	Global	2000–current	General regression neural networks (GRNNs)	Fraction of green vegetation cover
12–This study	MODIS, HJ-1	30 m, 15 days	China	2010	Pixel unmixing model	Fraction of green vegetation cover

Note: AVHRR: Advanced Very High Resolution Radiometer; SEVIRI: Spinning Enhanced Visible and Infrared Imager; MERIS: Medium Resolution Imaging Spectrometer; GIMMS: Global Inventory Modeling and Mapping Studies; QuikSCAT SIR: Quick Scatterometer images using the scatterometer image reconstruction algorithm; AMSR-E: Advanced Microwave Scanning Radiometer-Earth Observing System; TRMM: Tropical Rainfall Measuring Mission; MODIS: Moderate Resolution Imaging Spectroradiometer; TM: Thematic Mapper; ETM+: Enhanced Thematic Mapper.

proaches for retrieving and validating the FVC dataset and Section 4 reports our results. Discussion and concluding remarks are presented in Sections 5 and 6, respectively.

2. Study area and data

2.1 *Study area*

The study region includes mainland China and the island of Taiwan, covering over 9.6 million km^2. The climate over this region varies regionally and seasonally due to the East Asian monsoon and complex topography, which affects the spatial distribution of vegetation biomes (Fig. 1). The topography of China varies greatly from highly mountainous regions to inhospitable deserts and flat, fertile plains. It is analogous to a staircase descending from west to east. The main vegetation biomes in eastern China, including regions numbered 1, 2, 3, 4, 5, 7, 9, 12, and 14 in Fig. 1, are forests and cropland. Whereas, the dominant land cover types in western China, containing regions numbered 6, 8, 10, 11, and 13 in Fig. 1, are grassland, Gobi Desert, and saline-alkali land. Additionally, there are some artificial oases in regions 10 and 11, containing irrigated crops and pastures. The percentages of forests, cropland, grassland, and unused land (desert and bare soil) in China are 24.8%, 15.6%, 31.0%, and 23.2% in 2010, respectively (Zhang et al., 2014).

2.2 *In situ FVC measurements*

Time-series characteristics of the *in situ* FVC observations acquired at 22 FVC monitoring sites and the

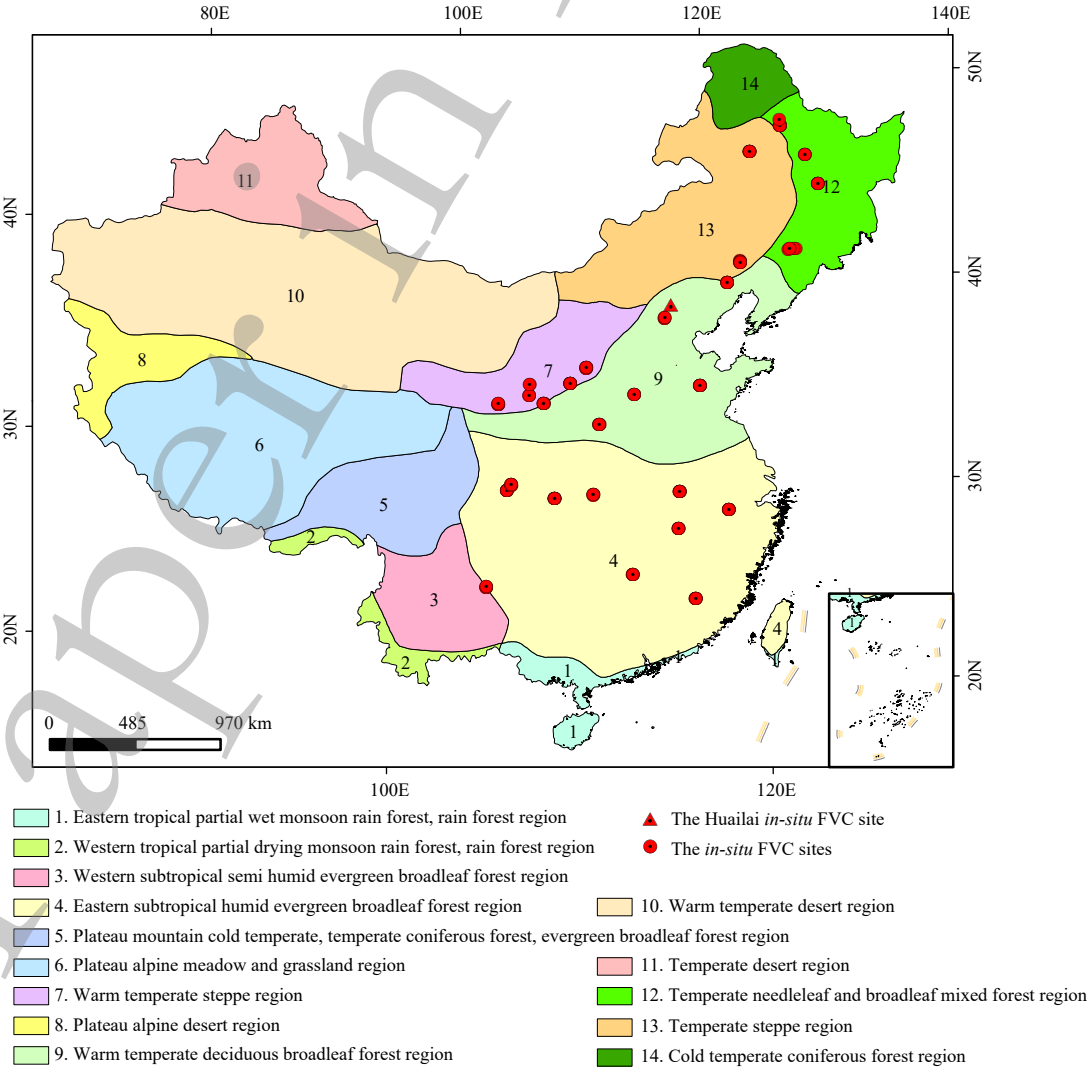

Fig. 1. The natural vegetation regionalization map of China; this represents ideal (or climax) vegetation if there was no human modification. The 14 vegetation regions are numbered. The solid red triangle and solid red circles represent the Huailai site and other 22 FVC monitoring sites, respectively.

Huailai experimental site are reported in Table 2 and their locations are provided in Fig. 1. The fortnightly measurements at 22 sites commenced in the first half month in January 2010 and ceased in the last half month in December 2010. The time series *in situ* measurements were used here to assess the seasonality of the FVC product. At Huailai experimental site, where the area is relatively homogeneous at a large scale, measurements were collected to assess the performance of the FVC products at 1-km resolution in Section 4.2. The characteristics of these FVC measurements are illustrated in Table 2.

2.2.1 *Time-series FVC measurements in small watersheds*

The time-series FVC measurements were conducted in 22 small watersheds mainly over eastern China, where denser vegetation is located compared to western China. The measurements served the First National Water Resource Survey of China in 2010 for the assessment of water erosion. In each watershed, five to seven sampling plots were chosen for FVC ground measurements over cropland, improved grassland, natural grassland, forest, and orchard. The number of sampling plots in each watershed depends on the richness of land cover types therein (Fig. 2). The measured FVC of a specific sampling plot would not be used if the surveyed land cover type differed from that delineated in the 30-m resolution land cover map (see Section 2.4.1). After filtering the plots which have mismatched land cover types, 97 sampling plots were available for validation (Table 2).

To measure *in situ* FVC, digital photos were acquired using a camera mounted on scaffolding. In each plot, five photos covering 15 m × 15 m were manually acquired for vegetation lower than 2 m. The FVC extraction method generally introduced an absolute error less than 5% (Yan et al., 2012). FVC of the sampling plot was calculated as the average of FVC derived from the five photos. The measurement frequency was once per 15 days, and hence there were 24 observations within the year at each FVC monitoring plot (Table 1).

For trees in the orchards and forests, we placed the digital camera between the overstory and understory, and then downward-looking photos were acquired from the portable scaffolding to characterize the understory vegetation, while extra upward-looking photos were acquired to capture the tree crown. The FVC was then obtained using:

$$\mathrm{FVC} = f_{\mathrm{up}} + (1 - f_{\mathrm{up}}) \cdot f_{\mathrm{down}}, \quad (1)$$

where f_{up} and f_{down} are the FVCs extracted from the photographs captured by the upward and downward photography, respectively.

2.2.2 *Measurements at a homogeneous region*

Huailai experimental site (40°21'N, 115°47'E) is located within a flat plain covering ~280 km^2. Summer corn covers more than 80% of the experimental region with other types of agriculture (e.g., fruit orchard, vineyard) covering the remaining ~20%. Measurements covered a complete growth cycle of corn (Zea mays) at 14 sampling plots that are each 30 m × 30 m (Table 2). FVC measured at a sampling plot can represent the FVC of a large homogeneous area. Ground measurements at this site were also obtained using the digital photography method as outlined above.

2.3 *Remote sensing data*

We used the HJ-1 multispectral reflectance, MODIS Nadir Bidirectional Reflectance Distribution Function (BRDF)-Adjusted Reflectance (NBAR) product (MCD43B4) and the corresponding quality description product (MCD43B2; https://lpdaac.usgs.gov/products/mcd43a4v006/), MODIS Land Cover Type product (MCD12Q1), and GEOV1 FVC product. The main dataset characteristics are summarized in Table 3. The HJ-1 multispectral reflectance, Collection 5 MCD43B4, MCD43B2, and MCD12Q1 were used to generate the high spatial resolution and high temporal frequency NDVI dataset and the GEOV1 FVC was used to train

Table 2. Characteristics of *in situ* FVC measurements used for validation

In situ FVC	Temporal coverage (year 2010)	Plot size	Number of plots (after quality control)
Time-series FVC	Every 15 days, 24 observations for each plot	60 m × 60 m	97
Huailai FVC	6 Jun, 19 Jun, 23 Jun, 2 Jul, 10 Jul, 20 Jul, 26 Sep	30 m × 30 m	14

Table 3. Characteristics of the remote sensing datasets

Dataset	Sensor	Spatial resolution and temporal frequency	Temporal extent
HJ-1 multispectral reflectance	*HJ-1A*/*1B*-CCD	30 m, 2 days	2010
MCD43B4	TERRA/AQUA-MODIS	1 km, 8 days	2005–2010
MCD43B2	TERRA/AQUA-MODIS	1 km, 8 days	2005–2010
MCD12Q1	TERRA/AQUA-MODIS	500 m, 1 year	2004
GEOV1 FVC	SPOT-VEGETATION	1/112°, 10 days	2010
GLASS FVC	TERRA/AQUA-MODIS, Landsat (TM, ETM+)	0.5 km, 8 days	2010

one of the coefficients of a nonlinear pixel unmixing model. Additionally, the GEOV1 FVC product and the Global Land Surface Satellite (GLASS) FVC product (Jia et al., 2015) were compared with the product over Huailai experimental site.

2.3.1 *HJ-1 multispectral reflectance*

The HJ-1 satellites (*HJ-1A* and *HJ-1B*; similar to Landsat in spectral band and spatial resolution) were launched in 2008. The HJ-1 multispectral surface reflectance data (post radiometric calibration and systematic geometric correction) were provided by China Centre for Resources Satellite Data and Application (http://www.cresda.com/EN/). The spatial resolutions of the red band and the near infrared (NIR) band are 30 m. The whole study region consists of 762 tiles with the size of 100 km ~north–south × 150 km ~east–west each. HJ-1 images were acquired three times during 2010 (the specific acquisition dates are not fixed). This dataset would be used to calculate instantaneous HJ-1 NDVI and to generate time-series NDVI for data fusion. The HJ-1 data are intensively selected from day-of-year (DOY) 90 to 310 in 2010 (Fig. 3) when vegetation changes more rapidly than the rest days of the year.

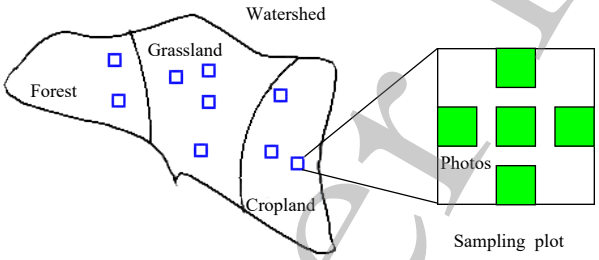

Fig. 2. Schematic diagram of a watershed, sampling plot, and digital photography.

2.3.2 *MODIS reflectance and land cover*

MODIS products we used were downloaded from the Land Processes Distributed Active Archive Center (LP-DAAC; https://lpdaac.usgs.gov/), including surface reflectance (MCD43B4 and MCD43B2) from 2005 to 2010 and land cover (MCD12Q1) in 2004. MCD43B4 is generated using a semi-empirical kernel-driven bidirectional reflectance model to rectify the actual view direction to the nadir direction (Lucht et al., 2000). Band 1 (red) and band 2 (NIR) were used to calculate the 1-km MODIS NDVI, which was used to form the background field for data fusion and to compute the coefficients of the nonlinear pixel unmixing model. MCD43B2 describes the overall quality of MCD43B4 using quality assessment (QA) values. Only pixels of highest quality for both two bands (QA = 0) were used here. MODIS land classification (MCD12Q1) is derived by a supervised decision-tree classification method (Channan et al., 2014). We merged the International Geosphere–Biosphere Programme (IGBP) (layer 1) categories to match the classification system of the 30-m national land use/cover (LC, hereafter) database of China introduced in Section 2.4.1. These two land cover datasets were used to acquire the area percentage of each land cover type within a MODIS pixel.

2.3.3 *GEOV1 FVC product*

The GEOV1 FVC product (distributed at http://land.copernicus.eu/global/products/FCover) is an improved version of the CYCLOPES FVC product, which was trained using an artificial neural network approach (Baret et al., 2013). The GEOV1 FVC product performed well when assessing FVC dynamics (i.e., showing reliable spatial distribution and smooth temporal profiles; Camacho et al., 2013), although there is still relatively high residual uncertainty (about 0.1 for croplands; Mu et al.,

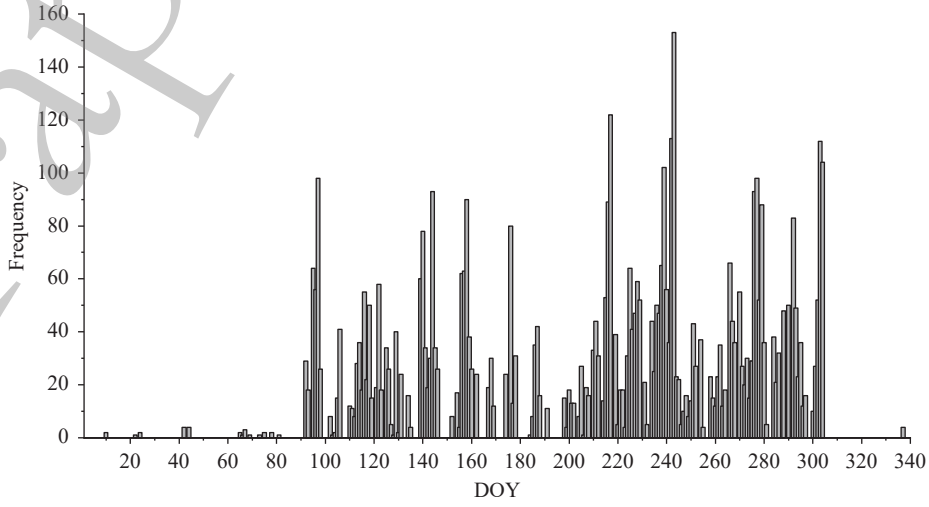

Fig. 3. The DOY frequency distribution of the collected HJ-1 multispectral reflectance data.

2015). In this paper, it was only used to fit the nonlinear trend of the nonlinear pixel unmixing model (Section 3.2.2) and compare with the generated FVC product.

2.3.4 *GLASS FVC product*

The GLASS FVC product was generated from MODIS surface reflectance by training regression neural networks with Landsat TM/ETM+ data. The spatial and temporal continuity of the GLASS FVC product were superior to the GEOV1 FVC product (Jia et al., 2015). We used the GLASS FVC product (distributed at http://www.geodata.cn/datapplication/OrderStepList.html) to validate the proposed product over Huailai experiment site.

2.4 *Auxiliary data*

2.4.1 *30-m resolution land cover data*

An all-China 30-m land cover dataset was updated in 2010 using visual interpretation based on professional field-based ecological knowledge. The input data included Landsat TM images with 30-m spatial resolution and, as alternative, the 20-m China-Brazil Earth Resources Satellite (CBERS) data and the 30-m HJ-1 data. The accuracy of the land cover data is about 95.41% (Zhang et al., 2014). Land cover data were used to provide the land cover type of each 30-m resolution pixel, and to acquire the area percentages of land cover types in MODIS pixels.

2.4.2 *Vegetation regionalization*

Vegetation regionalization is a theoretical integration of vegetation studies, mainly based on principles of geographical distribution of vegetation types (Zhang, 1993). It shows the regional distribution and the zonal differentiation of vegetation, and further indicates the regularity of the distribution of vegetation and its relationship with the environment. Chinese vegetation regions were obtained from Wang and Zuo (2010) and numbered from 1 to 14 (Fig. 1). The 14 vegetation regions (Fig. 1) are the basic units to calculate NDVI background and coefficients that transform NDVI into FVC.

3. Methods

We employed the CC data assimilation method and a nonlinear pixel unmixing model (Cai et al., 2011) to estimate the high spatial resolution and high temporal frequency FVC product using MODIS NBAR product, HJ-1 reflectance data, and GEOV1 FVC product respectively for each land cover type and each vegetation region. Figure 4 shows the general processes of the algorithm: acquisition of the high spatial resolution and high temporal frequency NDVI dataset (30-m NDVI, hereafter), training of the transformation coefficients from NDVI to FVC for different vegetation regions and land cover types, and the calculation and validation of FVC, corresponding to the following Sections, 3.1, 3.2, and 3.3, respectively.

3.1 *Generation of high spatial resolution and high temporal frequency NDVI*

The 30-m NDVI dataset was acquired using the CC data assimilation method. We used HJ-1 NDVI as the high resolution input data, and 8-day multi-year (2005–2010) averaged MODIS NDVI time series as the background data (Cai et al., 2011) that represent vegetation phenology for different land cover types.

3.1.1 *HJ-1 NDVI and MODIS NDVI time series*

NDVI is one of the most frequently used vegetation indices to characterize the vegetation status, defined by Eq. (2). HJ-1 NDVI and MODIS NDVI were respectively derived from HJ-1 multispectral reflectance data in 2010 and the MCD43B4 product during 2005–2010.

$$\mathrm{NDVI} = \frac{\rho_{\mathrm{NIR}} - \rho_{\mathrm{R}}}{\rho_{\mathrm{NIR}} + \rho_{\mathrm{R}}}, \tag{2}$$

where ρ_{R} and ρ_{NIR} are the reflectance of the red band and NIR band.

The geo-registered MCD12Q1 and 30-m land cover data were processed to output the area percentage image by computing the ratio of the number of high resolution pixels for a specific land cover type in a coarse pixel to the number of all high resolution pixels in this coarse pixel (Cai et al., 2011). Only the pixels with the area ratio greater than 95% (pure pixels, hereafter) were used. The multi-year averaged MODIS NDVI time series were acquired by averaging the 8-day-frequency MODIS NDVI time series over the six years, which were extracted over the pure pixels for each land cover type and vegetation region.

3.1.2 *High spatial resolution and high temporal frequency NDVI*

The CC method for data assimilation adopts the so called "index-then-blend" (i.e., calculate the index at both high and low spatial resolutions and then perform the blending operation) approach which produces more accurate results that the alternative "blend-then-index" approach (Jarihani et al., 2014), and can fully use the vegetation information from the two data sources simultaneously (Cai et al., 2011; Meng et al., 2011). The model can be expressed as:

$$X_{\mathrm{p}}(r_i) = X_{\mathrm{b}}(r_i) + \frac{\sum_{j=1}^{n} \varpi(r_i, r_j)[X_{\mathrm{h}}(r_j) - X_{\mathrm{b}}(r_j)]}{E_{\mathrm{h}}^2 / E_{\mathrm{b}}^2 + \sum_{j=1}^{n} \varpi(r_i, r_j)}, \tag{3}$$

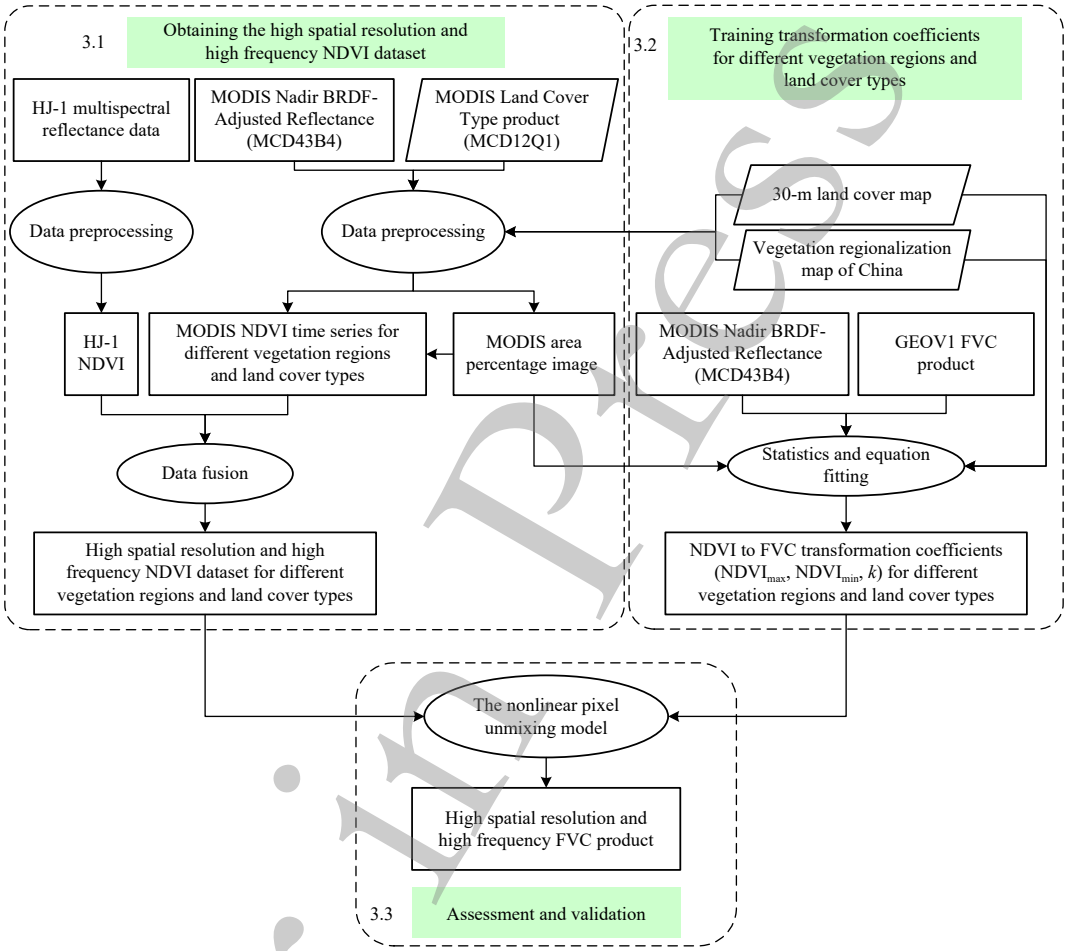

Fig. 4. Flowchart of the high spatial resolution and high temporal frequency FVC estimation. Remotely sensed data are shown in rectangles, land-cover vegetation products in parallelograms, and processes in ellipses. The numbers 3.1, 3.2, and 3.3 refer to the level 2 sub-headings of the Methods Section.

$$\varpi(r_i, r_j) = \mathrm{abs}[r_i - \mathrm{abs}(r_i - r_j)]/r_i, \quad (4)$$

where X_p, X_b, and X_h are the predicted NDVI, background field NDVI, and the high resolution input NDVI, respectively; r_i and r_j are the prediction date and the observation date, respectively; E_h^2 and E_b^2 are the errors of the high resolution input and background field data, respectively; n is the number of high resolution inputs; and $\varpi(r_i, r_j)$ is the weighting factor calculated by the time distance between background and high resolution input data.

The fused NDVI series for a 30-m pixel was generated at a 15-day frequency with the inputs of high resolution HJ-1 NDVI acquired three times in 2010, background field NDVI (i.e., the multi-year averaged NDVI time series for the vegetation region and land cover type), and the weighting factors. Water body was masked by using land cover types in FVC retrieval. The pixels with snow were not excluded from the HJ-1 NDVI data as the FVC values of snow pixels are generally calculated to be zero given low values of snow NDVI.

3.2 *Transformation coefficients and FVC estimation*

3.2.1 *Nonlinear pixel unmixing model*

The pixel unmixing model with two endmembers is the simplest and most extensively applied model in the various linear unmixing models (Yan et al., 2012). It assumes that each pixel consists of green vegetation and non-green background. The information (vegetation indices or spectral) of the pixel results from the linear weighted synthesis of the two components. The weight of each component is the area proportion of each component in the pixel. The vegetation proportion is the FVC of the pixel, which can be mathematically expressed as (Gutman and Ignatov, 1998):

$$\mathrm{FVC} = \frac{\mathrm{NDVI} - \mathrm{NDVI_s}}{\mathrm{NDVI_v} - \mathrm{NDVI_s}}, \quad (5)$$

where FVC is the proportion of vegetation area in the mixed pixel, namely, the FVC of the mixed pixel; NDVI

is the NDVI of the mixed pixel; and $NDVI_v$ and $NDVI_s$ are the NDVI of fully covered green vegetation and non-green background, respectively. This pixel unmixing model is a linear transformation between NDVI and FVC.

Lu et al. (2003) showed that NDVI was suitable to model FVC. Some studies defined the scaled NDVI [N^*, Eq. (6)] and established an identical quadratic relation between the scaled NDVI and FVC [Eq. (7); Choudhury et al., 1994; Carlson and Ripley, 1997]:

$$N^* = \frac{\mathrm{NDVI} - \mathrm{NDVI_s}}{\mathrm{NDVI_v} - \mathrm{NDVI_s}}, \tag{6}$$

$$\mathrm{FVC} \approx N^{*2}. \tag{7}$$

It is documented that the linear relationship or the quadratic relationship could reveal good agreement between NDVI and FVC in some cases (Xiao and Moody, 2005; Jiapaer et al., 2011). Instead of using a simple linear or quadratic expression to calculate FVC, an empirical nonlinear function is used to convert NDVI to FVC, which is appropriate for both the linear and quadratic forms (Mu et al., 2015). This model is defined as the nonlinear pixel unmixing model:

$$\mathrm{FVC} = \left(\frac{\mathrm{NDVI} - \mathrm{NDVI_s}}{\mathrm{NDVI_v} - \mathrm{NDVI_s}}\right)^k, \tag{8}$$

where FVC and NDVI are the FVC and NDVI of the mixed pixel, respectively; $NDVI_v$ and $NDVI_s$ are the NDVI of fully covered green vegetation and non-green background, respectively; and k is the linearity coefficient of the model.

3.2.2 *Transformation coefficients of the model*

It has long been known that $NDVI_v$ and $NDVI_s$ are biome-specific (Gutman and Ignatov, 1998; Zeng et al., 2000; Montandon and Small, 2008; Wu et al., 2014). The $NDVI_v$ depends upon the vegetation type, geometric structure, chlorophyll content, and physiology (mesophyll) of vegetation (Price, 1992; Carlson and Ripley, 1997). The $NDVI_s$ is affected by soil reflectance varying with soil types and soil moisture (O'Neill, 1994; Post et al., 2000; Lobell and Asner, 2002; Montandon and Small, 2008). In addition, k varies according to surface heterogeneity and vegetation type (Mu et al., 2015). Thus, the three coefficients were independently trained for each vegetation region and land cover type over the pure pixels.

The $NDVI_v$ and $NDVI_s$ can be estimated as maximum and minimum NDVI (i.e., $NDVI_{max}$ and $NDVI_{min}$) in the study areas based on the assumption that fully covered vegetation and non-vegetation background exist in the observed time and space (Gutman and Ignatov, 1998). They were determined through spatial and temporal statistical analysis of the 30-m NDVI data, assuming that similar $NDVI_{max}$ and $NDVI_{min}$ could be obtained for each vegetation region (see Fig. 1) and each land cover type. We re-grouped the land cover types into three main vegetation types: forest, cropland, and grassland in each region. This was performed in three steps. First, the annual maximum NDVI and minimum NDVI of the 30-m NDVI within the extent of the MODIS pure pixels were calculated. Second, the cumulative histogram of the annual maximum NDVI was acquired for the three main vegetation types in each region. The $NDVI_{max}$ was taken as the value at 75% of the cumulative histogram for cropland and grassland, and 90% for forest (Zeng et al., 2000). Third, and finally, the averaged value of the annual minimum NDVI for each vegetation type in each vegetation region was defined as the corresponding $NDVI_{min}$ (Wu et al., 2014; Ding et al., 2016). If these three steps fail to meet the criteria for $NDVI_{max}$ ($0.70 < NDVI_{max} < 0.95$) or $NDVI_{min}$ ($0.05 < NDVI_{min} < 0.20$), 0.84 and 0.07 are assigned to $NDVI_{max}$ and $NDVI_{min}$, respectively (Montandon and Small, 2008). The k describes the degree of nonlinearity and was acquired by fitting Eq. (8) with GEOV1 FVC and MODIS NDVI. GEOV1 FVC can reflect the general trends of vegetation growth (Camacho et al., 2013; Ding et al., 2015) and thereby provides reasonable information for the prediction of k.

3.2.3 *High spatial resolution and high temporal frequency FVC generation*

The FVC product was generated at 30-m resolution and 15-day frequency for different vegetation regions and land cover types by inputting the 30-m NDVI and the transformation coefficients to the nonlinear pixel unmixing model [Eq. (8)].

3.3 *Assessment and validation*

Assessment and validation of the high spatial resolution and high temporal frequency FVC product were completed through direct validation and inter-comparison. The direct validation was conducted using the *in situ* FVC measurements at 97 sampling plots in 22 small watersheds and 14 sampling plots at Huailai experimental site to quantify the overall performance of the product. The inter-comparison was carried out between the estimated FVC using the method proposed in Sections 3.1 and 3.2 and GEOV1 FVC product to analyze their spatial and temporal consistency.

3.3.1 *Direct validation*

The direct validation was conducted over 22 small watersheds and the Huailai experimental site (Fig. 1). To re-

duce the potential geo-location errors between the estimated FVC product and the field FVC measurements, we averaged the FVCs of 3 × 3 pixels (each 30-m resolution) centered on the ground point positioning pixel as suggested by Weiss et al. (2007). The bias of the estimated FVC over a sampling plot was calculated as:

$$\text{bias} = \text{FVC}_\text{e} - \text{FVC}_\text{r}, \tag{9}$$

where FVC_e is the averaged FVC over the 3 × 3 pixels, and FVC_r is the *in situ* FVC.

The GEOV1 FVC and GLASS FVC were also compared against the field FVC measurements over the Huailai experimental site.

3.3.2 *Inter-comparison with GEOV1 FVC*

The estimated FVC product was respectively mosaicked and resampled to the 1-km spatial resolution and then together with the GEOV1 FVC was monthly synthesized with the arithmetic mean to ensure they have the same temporal compositing periods for inter-comparison.

We evaluated the performance of the two products in four ways, including assessing: (i) the spatial and temporal distribution patterns; (ii) differences between the values of the estimated FVC and GEOV1 FVC; (iii) the correlation between the two products; and (iv) the spatial continuity represented by the percentage of missing values. Five statistical metrics, namely, DIFF, Ratio, mean error (ME), root-mean-square deviation (RMSD), and the Pearson correlation coefficient (R), were computed using the estimated FVC product and the GEOV1 FVC product per pixel over China for 2010; see Eqs. (10–14):

$$\text{DIFF}_{(i)} = \text{FVC}_{\text{e}(i)} - \text{FVC}_{\text{GEO}(i)}, \tag{10}$$

$$\text{Ratio}_{(i)} = \frac{\text{FVC}_{\text{e}(i)}}{\text{FVC}_{\text{GEO}(i)}}, \tag{11}$$

$$\text{ME} = \frac{\sum_{i=1}^{n} \text{DIFF}_{(i)}}{n}, \tag{12}$$

$$\text{RMSD} = \sqrt{\frac{\sum_{i=1}^{n} \text{DIFF}_{(i)}^2}{n}}, \tag{13}$$

$$R = \frac{\sum_{i=1}^{n} (\text{FVC}_{\text{e}(i)} - \overline{\text{FVC}}_\text{e})(\text{FVC}_{\text{GEO}(i)} - \overline{\text{FVC}}_\text{GEO})}{\sqrt{\sum_{i=1}^{n} (\text{FVC}_{\text{e}(i)} - \overline{\text{FVC}}_\text{e})^2 \sum_{i=1}^{n} (\text{FVC}_{\text{GEO}(i)} - \overline{\text{FVC}}_\text{GEO})^2}}, \tag{14}$$

where $\text{FVC}_{\text{e}(i)}$ and $\text{FVC}_{\text{GEO}(i)}$ are respectively the estimated FVC and GEOV1 FVC of a pixel at ith temporal phase; $\overline{\text{FVC}}_\text{e}$ and $\overline{\text{FVC}}_\text{GEO}$ represent the averaged estimated FVC and the averaged GEOV1 FVC of the pixel, respectively; and n is the number of valid FVCs for the pixel (the number of valid temporal phases), which means that missing values do not contribute to n.

4. Results

4.1 *Spatial distribution of the estimated FVC product*

Figures 5a–c show the spatial distribution of forests, cropland, and grassland, respectively. The sub-classes under the three main land cover types were specifically defined by Zhang et al. (2014). Forest, shrub, and sparse woods, respectively, consist of trees higher than 2 m with canopy cover greater than 30%, trees less than 2 m in height with canopy cover greater than 40%, and trees with canopy cover of 10%–30%. Other woods represent tea gardens, orchards, groves, and nurseries. Paddy field represents the cropland that has sufficient water supply for planting paddy rice and lotus, while dry land only provides limited irrigation facilities for rain-fed farming crops. Sparse grass, moderate grass, and dense grass, respectively, were the grassland with canopy cover between 5% and 20%, between 20% and 50%, and greater than 50%.

Forests are mainly distributed in Northeast and Southeast China (Fig. 5a), with cropland mainly distributed in central and eastern China and oasis in Northwest China (Fig. 5b), and grasslands are mainly distributed in northern China (Inner Mongolia), oasis in Northwest China, and southwestern Tibetan Plateau (Fig. 5c). FVC of forests is generally higher than that of cropland, and the FVC of cropland is higher than that of grassland. There are large deserts in Northwest China (Fig. 1), which have FVC values of almost zero. It means that China's FVC ascends from west to east with FVC approximately from 0 to 1, while the FVC in the oasis class in Northwest China is higher than that of the surrounding regions. The spatial distribution pattern of the annual maximum FVC over China (Fig. 5d) is in agreement with the actual situation which is substantially affected by East Asian monsoon and China's topography (Hu and Zhang, 2006). The water bodies were masked (e.g., Fig. 5d).

4.2 *Direct validation*

Figure 6 shows the systematic differences between the *in situ* FVC measurements and the estimated FVC product during 2010 for all FVC monitoring sites in the 22 small watersheds. The basic statistics of the time series bias throughout the whole year are presented with mean and ± 1 standard deviation in Fig. 6. The bias of the estimated FVC product over cropland (Fig. 6b)

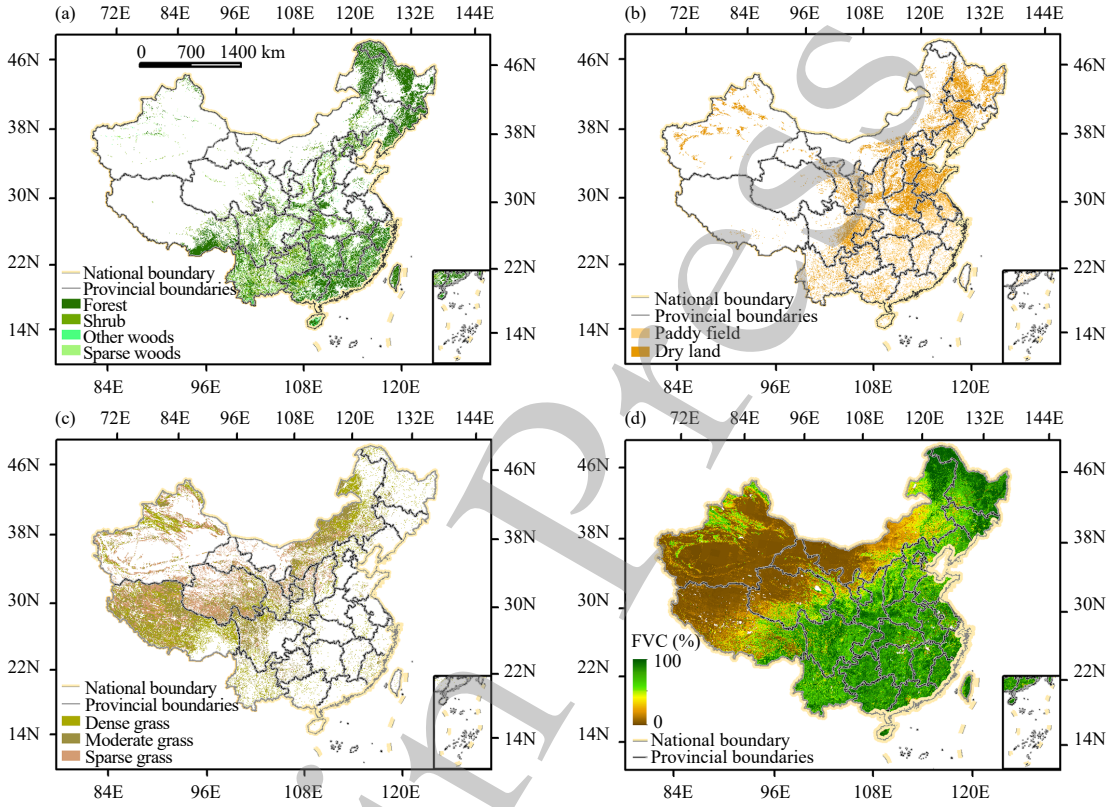

Fig. 5. The spatial distributions of the three main vegetation types and the annual maximum FVC over China in 2010. Sub-plot (a) provides locations of forests, (b) cropland, and (c) grassland, with (d) reporting the annual maximum FVC.

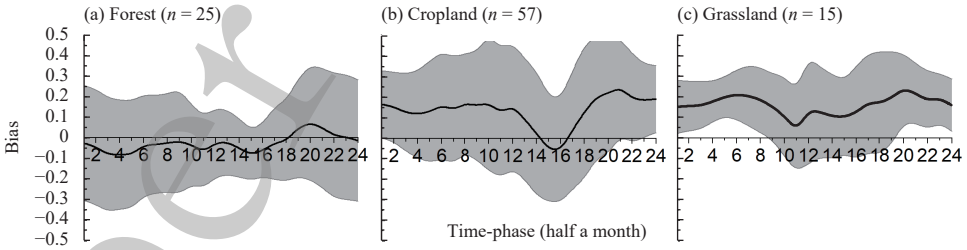

Fig. 6. The mean bias of the estimated FVCs over FVC monitoring sites for each temporal phase and vegetation type in 2010. Figures 6a–c represent the results over forests, cropland, and grassland, respectively; *n* is the number of measurements involved in the results. The black curves are the time series of mean bias at each half a month, commencing in January 2010. The upper and lower boundaries of the grey ribbon are determined by adding a negative and positive standard deviation, respectively, to the mean bias.

presents a temporal fluctuation with a general trend of overestimation, while a slight underestimation is found for July and August. The bias over grassland also shows overestimation (Fig. 6c), and the mean bias of the forest FVC is relatively small with the range from −0.081 to 0.075 (Fig. 6a).

All *in situ* FVC measurements over Huailai experiment site were used to validate the proposed method. A good agreement (R^2 = 0.809, RMSD = 0.065) is observed between the FVC estimates and the ground measurements (Fig. 7). The performance of the proposed FVC is comparable to the GEOV1 FVC (R^2 = 0.612, RMSD = 0.100), and the GLASS FVC (R^2 = 0.713, RMSD = 0.110).

4.3 *Inter-comparison*

Figure 8 shows the seasonal FVC distributions across China from the HJ-1/MODIS-based blending method developed here and the GEOV1 FVC product. January, April, July, and October represent the seasonal FVCs in winter, spring, summer, and autumn, respectively. A good spatial and temporal distribution agreement between the two products is observed. The seasonal distribution shows reasonable temporal pattern: the high FVC values in summer (Figs. 8c, g) and the relatively low FVC values in winter (Figs. 8a, e). Some differences

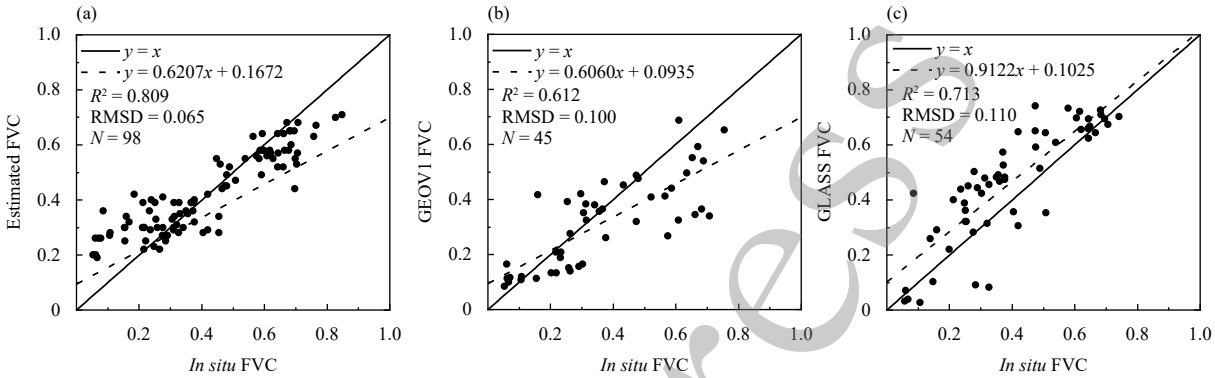

Fig. 7. Scatterplot of the estimated FVC and *in situ* FVC measurements in Huailai experimental site. The dominant land cover type is cornfield (comprising more than 80% of the experimental region). Cropland also includes the deciduous orchard (covering the remaining 20% of the experimental region).

between the two FVC products exist in spring (Figs. 8b, f), when the change of vegetation is more rapid than the other seasons (Xie and Wilson, 2020) and would cause more uncertainty due to the temporal compositing period (1 month for GEOV1 FVC and half a month for the proposed FVC). The FVC values of snow- or ice-covered land and lakes are zero due to their low NDVI values. Figure 9 presents the seasonal variation of the difference between the estimated FVC and the GEOV1 FVC, and the ratio of these two products. It is prominent that there are invalid values in GEOV1 FVC maps (percentages are shown in the legends of Fig. 8), whereas no invalid values exist in all the estimated FVC maps (with the water mask).

The monthly time series results of the two FVC products over all pure pixels for the cropland, forests, and grassland (Figs. 10a–c) reveal that both products capture the seasonal phenological variation. The FVC is low and has almost no variation in winter and spring (October to March) when the vegetation stops growing or grows very slowly. Then the FVC increases gradually in spring (April) when the vegetation starts growing. Then, the FVC reaches the maximum value in summer (July) when the vegetation is flourishing (as limited drought conditions were experienced across China in 2010). Finally, the FVC decreases gradually to the minimum value due to the vegetation decaying and dying.

The two products are relatively consistent in their temporal variation trends; however, there are some important differences. Figure 10a shows that for forests for the GEOV1 FVC product there is a bimodal distribution, with a small local maxima being estimated in February which is not consistent with *in situ* observations. For cropland (Fig. 10b), the maxima of the estimated FVC developed here occur about a month prior to the maxima in the GEOV1 FVC product, and importantly for crop yield estimation (that is typically related to the growing-season integral), the estimated FVC has higher values for longer (i.e., it is broader) when compared to the GEOV1 FVC product. Additionally, there exist some differences in magnitude; for example, the estimated FVC is systematically higher than GEOV1 FVC product by up to 0.1 throughout the year for grassland (Fig. 10c).

No missing value was observed in the estimated FVC product because gaps in HJ-1 images were filled with MODIS data in the fusion and generation of NDVI dataset. In contrast, Fig. 8 shows that the GEOV1 FVC (i.e., the preprocessed SPOT-VEGETATION reflectance data) contained numerous missing values (Camacho et al., 2013). Figure 11a shows the percentage map of the missing values of GEOV1 FVC products in 2010. However, the VEGETATION biogeophysical product version 2 (GEOV2) used climatology information from version 1 to apply temporal smoothing and gap filling to improve spatial and temporal continuity and consistency (Verger et al., 2014).

Maps of the calculated statistical metrics R, ME, and RMSD between the time series of estimated FVC and GEOV1 FVC products in 2010 are shown in Figs. 11b–d, respectively. Figure 11b indicates that prominent positive correlations ($0.8 \leqslant R \leqslant 1$) between the two FVC products are observed in most of the eastern China. The negative correlations and weak correlations (−0.2 to 0.2) are found in the desert areas in Northwest China and the Tibetan Plateau, where FVC remains low (< 0.1) all year.

A good agreement between the estimated FVC and the GEOV1 FVC products was observed with the annual ME mainly distributed from −0.1 to 0.1 (Fig. 11c). The spatial distributions of RMSD between the estimated FVC product and the GEOV1 FVC product agree with that of the annual maximum FVC in Fig. 11d. This means that the regions with low FVC values have low RMSD val-

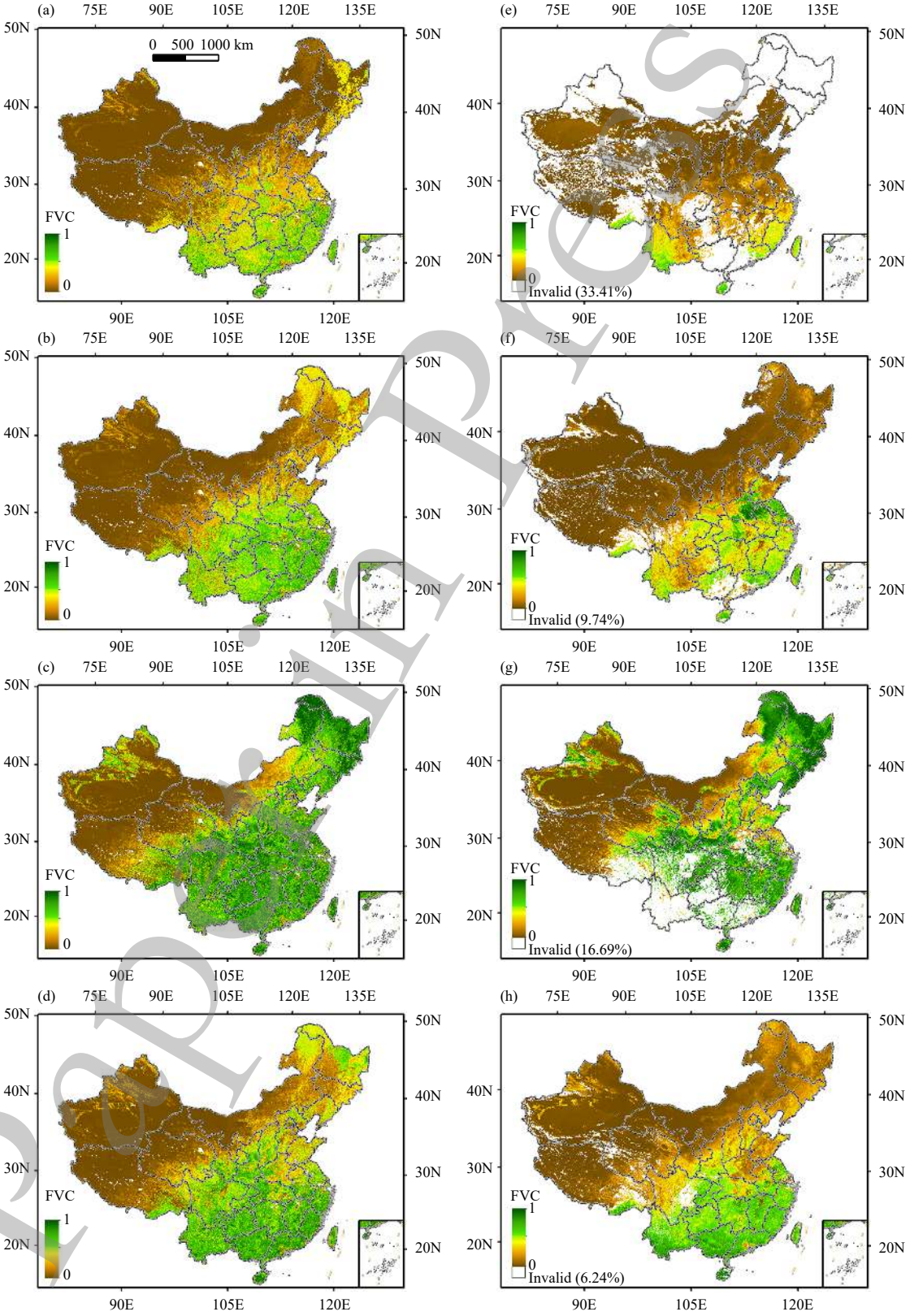

Fig. 8. The seasonal spatial distributions of the estimated FVC product developed herein (left column) and the GEOV1 FVC product (right column). Sub-plots (a) to (d) are January, April, July, and October, respectively, for the estimated FVC product. Sub-plots (e) to (h) are the corresponding monthly GEOV1 FVC estimates. The numbers in parenthesis directly to the right of the word "Invalid" in the legend report the percentage area of China (9.6×10^6 km^2) containing invalid (or unavailable) pixels each month. Note there is never any invalid FVC estimates in the product developed herein.

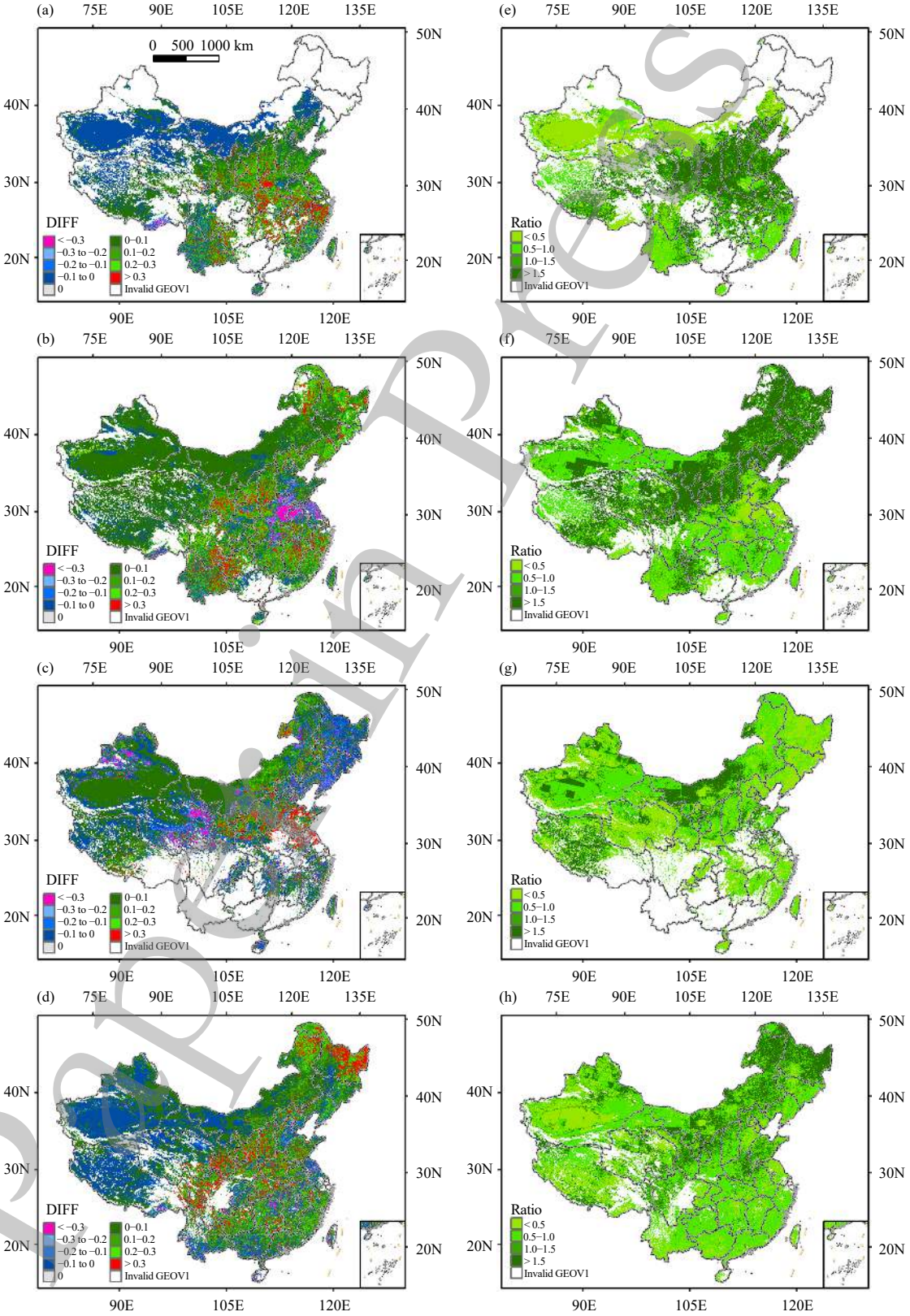

Fig. 9. The seasonal variations of the difference between the estimated FVC product (left column) and the GEOV1 FVC product (right column). Sub-plots (a) to (d) are January, April, July, and October, respectively, for the differences between the estimated FVC and GEOV1 FVC. Sub-plots (e) to (h) are the corresponding ratios of the estimated FVC to GEOV1 FVC. White areas on each show where GEOV1 FVC estimates were invalid.

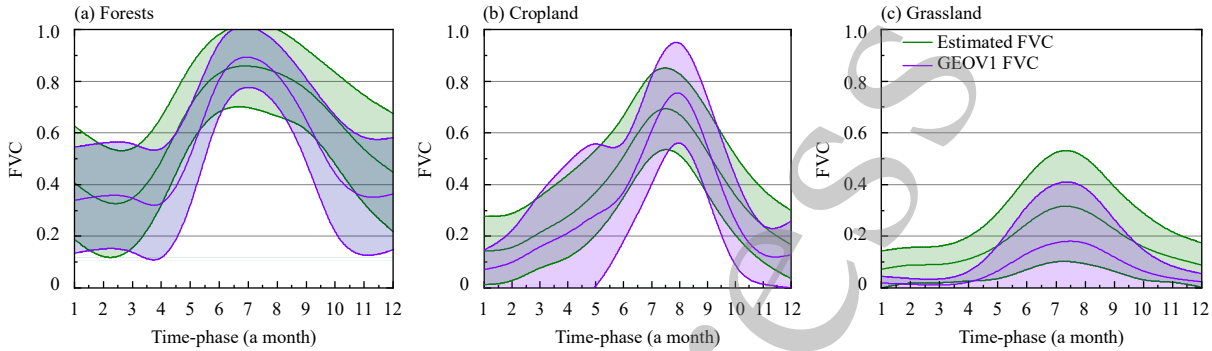

Fig. 10. Seasonal variations of mean values of the estimated FVC and GEOV1 FVC products over all pure pixels within 2010 for the three main vegetation types (provided by the solid line). The basic datasets for statistics were the monthly composed FVC products. The width of ribbon belt represents ± 1 standard deviation from the mean.

ues and high overall accuracy and vice versa. The regions with large RMSDs are almost consistent with the regions with the large missing data percentage of the GEOV1 FVC product, which means that the RMSD values are partly influenced by the amount and the quality of data involved in GEOV1 FVC product calculation.

4.4 *Sensitivity of FVC to $NDVI_{max}$ and $NDVI_{min}$*

The accuracy of the FVC estimate is influenced by the accuracy of $NDVI_{max}$, $NDVI_{min}$, and k according to Eq. (8). We only analyzed the influences of the $NDVI_{max}$ and $NDVI_{min}$ on the estimation of FVC (Fig. 12), because the coefficient k is very close to 1, and its variation is negligible. The NDVI varies from 0 to 1 with a sampling interval of 0.2. For each NDVI, the changing ranges of $NDVI_{max}$ and $NDVI_{min}$ were set from 0.7 to 0.95 and from 0.05 to 0.2, respectively, with 0.05 as the sampling interval, which were determined according to previous studies (Gutman and Ignatov, 1998; Zeng et al., 2000; Montandon and Small, 2008; Jiménez-Muñoz et al.,

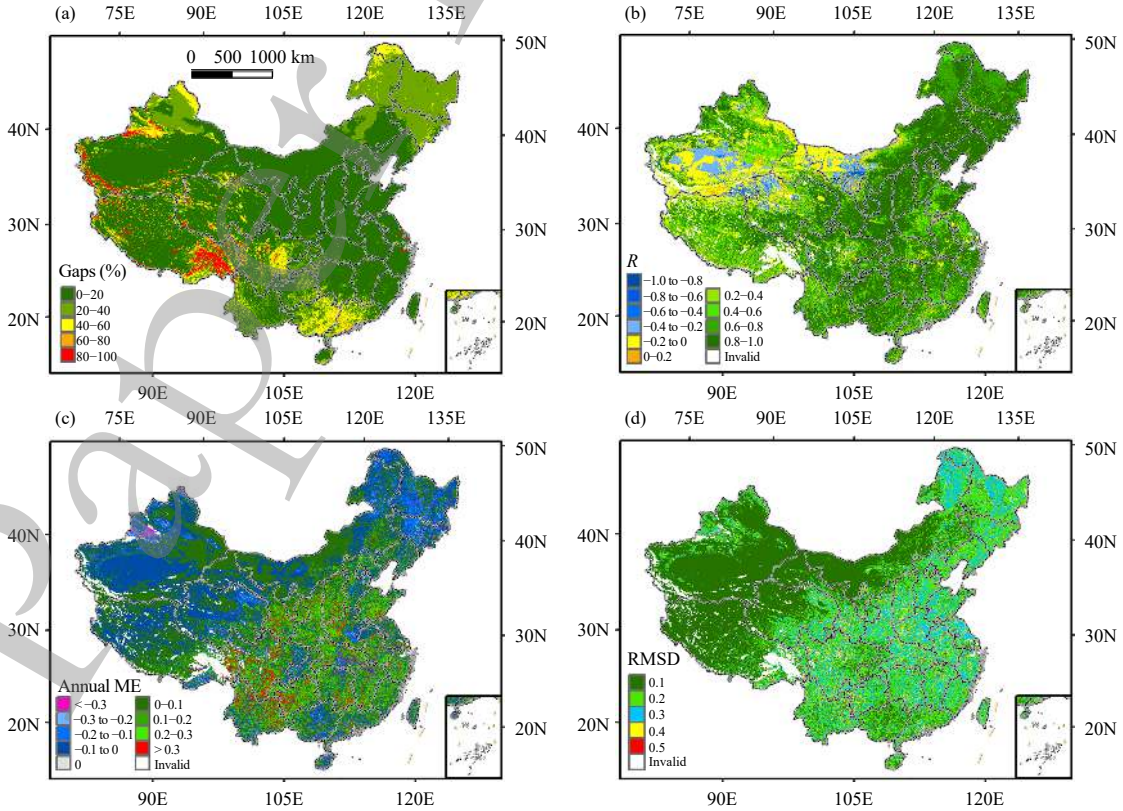

Fig. 11. Statistical characteristics and assessment between the estimated FVC and GEOV1 FVC products in 2010 over China. Sub-plot (a) shows the percentage of annual missing values of GEOV1 FVC, (b) is the map of R values, ranging from +1.0 to −1.0, (c) reports the annual ME, and (d) reports the RMSD.

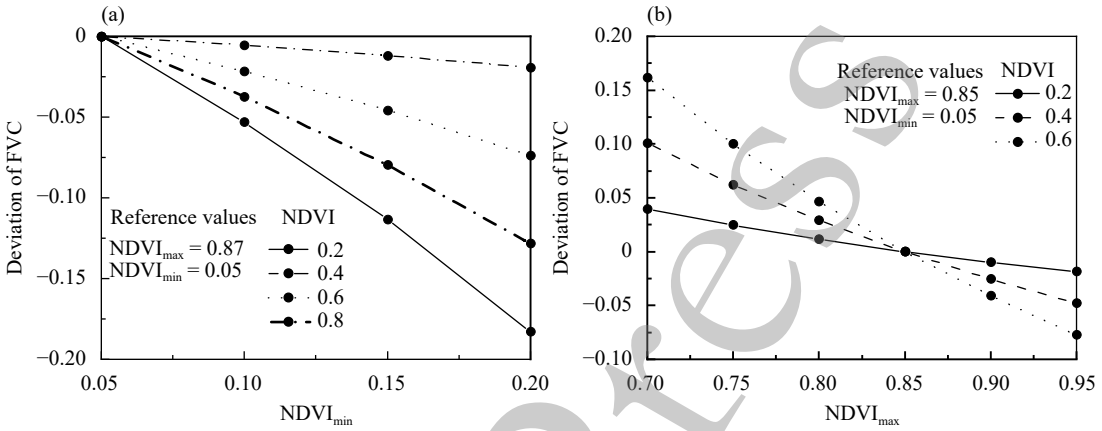

Fig. 12. The deviations of FVC estimate using the method developed herein with the variation of $NDVI_{min}$ and $NDVI_{max}$. (a) The influence of $NDVI_{min}$ and (b) the influence of $NDVI_{max}$.

2009; Wu et al., 2014) and the boundary conditions in Section 3.2.2. The reference values of $NDVI_{max}$ and $NDVI_{min}$, i.e., the values to calculate the reference FVC, were set close to the values used in this study when analyzing the influences of $NDVI_{min}$ (Fig. 12a) and $NDVI_{max}$ (Fig. 12b). The deviations of FVC were obtained with the changes of $NDVI_{max}$ and $NDVI_{min}$. In Fig. 12a, we could see that the FVC decreased with the increase of $NDVI_{min}$, and that the effect of $NDVI_{min}$ on FVC would be greater when the NDVI was smaller. When the NDVI was 0.2, the influence of $NDVI_{min}$ on FVC was the largest among our research, and the deviation of FVC from the reference was up to −0.2. Similarly, we could see in Fig. 12b that the FVC presented a decrease trend with the increase of $NDVI_{max}$.

5. Discussion

5.1 *Fusion of high resolution and high frequency data*

The fusion of high resolution and high frequency data combines the "beneficial" characteristics of each input data types. The output of high frequency temporal changes with high spatial detail enables monitoring vegetation phenology with fine resolutions (Singh et al., 2011; Bhandari et al., 2012; Walker et al., 2014; Zhang and Wu, 2015). Another strategy to generate high resolution and high frequency data is to fill the gaps in high resolution data by using interpolation techniques (Yang et al., 2017). However, high resolution satellites revisit the same place with longer time intervals. Landsat data are acquired every 16 days, causing large gaps due to the cloudiness especially in South China (Wilson and Jetz, 2016; Cai et al., 2017). Therefore, the data fusion technique, such as that developed herein, generates products with better continuity in space and time (Fig. 8; Weiss et al., 2014). In addition, high resolution (30 m) data are rare especially before 2014, with the exception of Landsat. The data fusion with HJ-1 data (start from 2008) is important to generate long time series products as *Landsat-8*, Sentinel-2, and Chinese Gaofen satellites were launched after 2013. The method implemented on the fusion of MODIS and HJ-1 data (similar to Landsat in spectral band and spatial resolution) can help to generate a more continuous time-series FVC product.

We implemented the data fusion of NDVI with an "index-then-blend" manner, which is more accurate than a "blend-then-index" manner due to less error propagation (Jarihani et al., 2014). The NDVI blending method developed herein showed a deviation of approximately less than 0.1 from field measurements, better than or at least comparable to the widely used STARFM method (Cai et al., 2011). The uncertainty transferred to FVC will be less than 0.13 using Eq. (5) with $NDVI_v$ and $NDVI_s$ of default values (0.84 and 0.07 in Section 3.2.2).

However, the temporal frequency of the fused data primarily depends on the frequency of coarse resolution data that have shorter revisit time (Becker-Reshef et al., 2010). The MODIS NBAR product, composed of 16-day/1-km observations, was used as the background of NDVI in this study, as the product is free of angular effects. With the relatively low frequency of the background data, some discrepancies in the FVC estimates were expected. We found that the FVC had discrepancies up to 0.15 against the *in situ* FVCs in some time-phases in Fig. 6. The biases of the estimated FVC product over cropland (Fig. 6b) present relatively large uncertainty of FVC especially from October to December. For grassland, larger biases exist in the start and the end of the year. In Fig. 6, larger biases are also observed in the rapid change period of vegetation, e.g., March to

May, and September to October. Low frequency MODIS NBAR product can miss the temporal information when vegetation changes quickly, and induce errors to the 30-m NDVI dataset. Another issue that affects the performance of data fusion is the limited amount of Landsat-like high resolution data (Roy et al., 2008). For each location, HJ-1 images were only acquired at three temporal phases. The data acquisition dates are non-uniformly distributed in 2010 (Fig. 3). There is a small amount of imagery available for spring and winter when the vegetation changes would not be completely reflected in 30-m FVC as the primary information is only from the 1-km MODIS NDVI background data. The small amount of HJ-1 high resolution data used for the start and the end of the year could account for the discrepancies to some degree. It is expected that the accuracy of FVC can be promoted with more high spatial resolution observations.

The NDVI background data were selected from 6-yr (2005–2010) MODIS NDVI. The selection involved the QA provided by MODIS product, the correction of BRDF effect (MCD43B4), and the assessment of the spatial homogeneity using 30-m resolution land cover map (Section 2.3.2). We used MODIS land cover product in 2004 (Table 3) and 30-m resolution classification map in 2010 to exclude the influence of land cover changes over the years. Only the pixels with the same land cover type can be the background NDVI candidates.

The introduction of classification data benefits the accuracy of fused high resolution and high frequency data (Fu et al., 2013) with 30-m vegetation classification datasets becoming recently operational at the global scale (Gong et al., 2013; Chen et al., 2015). However, the misclassification of land cover types would degrade the quality of the retrieval of transformation coefficients from NDVI to FVC, particularly between categories with substantially different $NDVI_{max}$ and $NDVI_{min}$ (e.g., grasslands versus broadleaf forest; Zeng et al., 2000).

5.2 *Uncertainty in determining $NDVI_{max}$, $NDVI_{min}$, and linearity coefficient*

Neural network is popular in generating FVC product at a large scale (Table 1). Pixel unmixing model is also convenient to produce FVC product at regional or global scales whereas the determination of $NDVI_{max}$ and $NDVI_{min}$ is important. Figure 12 shows that the values of $NDVI_{min}$ and $NDVI_{max}$ mostly affect FVC estimates over sparse vegetation (low NDVI) and dense vegetation (high NDVI), respectively. The estimated FVC product overestimates FVC for grassland and cropland (Figs. 6, 10), and it may be caused by the uncertainty of $NDVI_{min}$. Xiao and Moody (2005) showed that the influence of the soil background would produce an overestimation of FVC in sparsely vegetated area. The overestimation of FVC would be larger than 0.2 when using the invariant $NDVI_{min}$ (about 0.05) compared to using the mean NDVI computed from field measured $NDVI_{min}$ (0.2 ± 0.1) (Montandon and Small, 2008). Similarly, the overestimation of FVC would be 0.07 ± 0.08 when the FVC was estimated using the invariant $NDVI_{min}$ (about 0.05) in Northeast China, and the largest error occurred at a low NDVI level (Ding et al., 2016). In our study, the NDVI of grassland is usually less than 0.4, which indicates that the uncertainty of $NDVI_{min}$ in this study would substantially affect the estimation of FVC. In addition, the reference FVC, say, *in situ* measurements and GEOV1 FVC, explains the relative overestimation of FVC for sparse vegetation to some degree: the number of sampling plots is not large over grassland (15 plots) and the underestimation of GEOV1 FVC is found on open grassland and sparse vegetation (Ding et al., 2015). The determination of $NDVI_{max}$ and $NDVI_{min}$ is expected to be improved by introducing physical model to avoid the uncertainty in statistical methods (Song et al., 2017; Mu et al., 2018).

In the proposed method, the linearity coefficient k is acquired by fitting Eq. (8) with GEOV1 FVC and MODIS NDVI, which is impacted by the quality of GEOV1 FVC and then may influence the estimated FVC. However, the fitted k was found to be approximately 1 and the linear relationship between NDVI and FVC was widely used in many applications (Gao et al., 2020), indicating that the uncertainty induced by k could be insignificant.

6. Conclusions

In this study, we proposed a retrieval algorithm for green FVC estimation at high spatial resolution and high temporal frequency by the combination of fine resolution images and high temporal frequency images. We chose the multi-year averaged MODIS NDVI time series as the background field and the HJ-1 NDVI as the high-resolution inputs for the CC data assimilation method for each vegetation region and each land cover type. Then, we used the produced high spatial resolution and high temporal frequency NDVI and statistically obtained transformation coefficients from NDVI to FVC to estimate an FVC product at 30-m/15-day resolution within 2010 over China. The comparison was implemented with *in situ* FVC measurements over 22 small watersheds of Chinese soil and water conservation monitoring station and a spatially homogeneous experiment site (Huailai).

Our product was consistent with the vegetation distribution in China in terms of the temporal and spatial distribution pattern of FVC and was very consistent with the ground-measured FVC over the Huailai site (R^2 = 0.809, RMSD = 0.065). FVC estimate does not deviate far from the time series measurements over 22 watersheds, especially for forest (less than 0.1). Furthermore, the FVC maps generated from the proposed method had a comparable spatial consistency with the GEOV1 FVC data, and a better temporal and spatial continuity.

In summary, the proposed method paves the way to operationally generate high spatial resolution and high temporal frequency FVC products using multisource data. However, there are still some limitations that need rectification for further application. Further work should focus on improving the product quality especially at important phenology periods of vegetation and the determination of coefficients in pixel unmixing model. The background NDVI time series can be extracted at a smaller scale, e.g., at the pixel scale of MODIS data, to capture more temporal information of vegetation.

Acknowledgments. We thank China Centre for Resources Satellite Data and Application for providing HJ-1 data, Resource and Environment Science and Data Center (RESDC) for providing the land cover data, the European Space Agency for providing free GEOV1 data, and the LP-DAAC and MODIS science team for providing free MODIS products. Thanks to Wenwen Cai, Shuai Huang, and Jingyi Jiang for the data processing. We thank Professor Wenbo Zhang for sharing the FVC on soil erosion in watersheds and Jun Chen for drawing some of the important figures. We especially appreciate the contribution from Academician Xiaowen Li. We thank the two reviewers and Editor for helpful comments that improved an earlier version of this paper.

REFERENCES

Bacour, C., F. Baret, D. Béal, et al., 2006: Neural network estimation of *LAI*, *fAPAR*, *fCover* and *LAI* × C_{ab}, from top of canopy MERIS reflectance data: Principles and validation. *Remote Sens. Environ.*, **105**, 313–325, doi: 10.1016/j.rse.2006.07.014.

Baret, F., O. Hagolle, B. Geiger, et al., 2007: LAI, fAPAR and fCover CYCLOPES global products derived from VEGETATION: Part 1: Principles of the algorithm. *Remote Sens. Environ.*, **110**, 275–286, doi: 10.1016/j.rse.2007.02.018.

Baret, F., M. Weiss, R. Lacaze, et al., 2013: GEOV1: *LAI* and *FAPAR* essential climate variables and *FCOVER* global time series capitalizing over existing products. Part1: Principles of development and production. *Remote Sens. Environ.*, **137**, 299–309, doi: 10.1016/j.rse.2012.12.027.

Becker-Reshef, I., C. Justice, M. Sullivan, et al., 2010: Monitoring global croplands with coarse resolution earth observations: The Global Agriculture Monitoring (GLAM) Project. *Remote Sens.*, **2**, 1589–1609, doi: 10.3390/rs2061589.

Bhandari, S., S. Phinn, and T. Gill, 2012: Preparing Landsat Image Time Series (LITS) for monitoring changes in vegetation phenology in Queensland, Australia. *Remote Sens.*, **4**, 1856–1886, doi: 10.3390/rs4061856.

Broxton, P. D., X. B. Zeng, W. Scheftic, et al., 2014: A MODIS-based global 1-km maximum green vegetation fraction dataset. *J. Appl. Meteor. Climatol.*, **53**, 1996–2004, doi: 10.1175/JAMC-D-13-0356.1.

Busetto, L., M. Meroni, and R. Colombo, 2008: Combining medium and coarse spatial resolution satellite data to improve the estimation of sub-pixel NDVI time series. *Remote Sens. Environ.*, **112**, 118–131, doi: 10.1016/j.rse.2007.04.004.

Cai, H. K., X. Feng, Q. L. Chen, et al., 2017: Spatial and temporal features of the frequency of cloud occurrence over China based on CALIOP. *Adv. Meteor.*, **2017**, 4548357, doi: 10.1155/2017/4548357.

Cai, W. W., J. L. Song, J. D. Wang, et al., 2011: High spatial-and temporal-resolution NDVI produced by the assimilation of MODIS and HJ-1 data. *Can. J. Remote Sens.*, **37**, 612–627, doi: 10.5589/m12-004.

Camacho, F., J. Cernicharo, R. Lacaze, et al., 2013: GEOV1: LAI, FAPAR essential climate variables and FCOVER global time series capitalizing over existing products. Part 2: Validation and intercomparison with reference products. *Remote Sens. Environ.*, **137**, 310–329, doi: 10.1016/j.rse.2013.02.030.

Carlson, T. N., and D. A. Ripley, 1997: On the relation between NDVI, fractional vegetation cover, and leaf area index. *Remote Sens. Environ.*, **62**, 241–252, doi: 10.1016/S0034-4257(97)00104-1.

Channan, S., K. Collins, and W. R. Emanuel, 2014: Global Mosaics of the Standard MODIS Land Cover Type Data. University of Maryland and the Pacific Northwest National Laboratory, College Park, Maryland, USA, 30 pp.

Chen, J., J. Chen, A. P. Liao, et al., 2015: Global land cover mapping at 30 m resolution: A POK-based operational approach. *ISPRS J. Photogr. Remote Sens.*, **103**, 7–27, doi: 10.1016/j.isprsjprs.2014.09.002.

Choudhury, B. J., N. U. Ahmed, S. B. Idso, et al., 1994: Relations between evaporation coefficients and vegetation indices studied by model simulations. *Remote Sens. Environ.*, **50**, 1–17, doi: 10.1016/0034-4257(94)90090-6.

DeFries, R. S., J. R. G. Townshend, and M. C. Hansen, 1999: Continuous fields of vegetation characteristics at the global scale at 1-km resolution. *J. Geophys. Res. Atmos.*, **104**, 16911–16923, doi: 10.1029/1999JD900057.

Ding, Y. L., X. M. Zheng, T. Jiang, et al., 2015: Comparison and validation of long time serial global GEOV1 and regional Australian MODIS fractional vegetation cover products over the Australian continent. *Remote Sens.*, **7**, 5718–5733, doi: 10.3390/rs70505718.

Ding, Y. L., X. M. Zheng, K. Zhao, et al., 2016: Quantifying the impact of $NDVI_{soil}$ determination methods and $NDVI_{soil}$ variability on the estimation of fractional vegetation cover in Northeast China. *Remote Sens.*, **8**, 29, doi: 10.3390/rs8010029.

Donohue, R. J., T. R. McVicar, and M. L. Roderick, 2009: Cli-

mate-related trends in Australian vegetation cover as inferred from satellite observations, 1981–2006. *Glob. Change Biol.*, **15**, 1025–1039, doi: 10.1111/j.1365-2486.2008.01746.x.

Emelyanova, I. V., T. R. McVicar, T. G. Van Niel, et al., 2013: Assessing the accuracy of blending Landsat–MODIS surface reflectances in two landscapes with contrasting spatial and temporal dynamics: A framework for algorithm selection. *Remote Sens. Environ.*, **133**, 193–209, doi: 10.1016/j.rse.2013.02.007.

Fu, D. J., B. Z. Chen, J. Wang, et al., 2013: An improved image fusion approach based on enhanced spatial and temporal the adaptive reflectance fusion model. *Remote Sens.*, **5**, 6346–6360, doi: 10.3390/rs5126346.

Gan, M. Y., J. S. Deng, X. Y. Zheng, et al., 2014: Monitoring urban greenness dynamics using multiple endmember spectral mixture analysis. *PLoS ONE*, **9**, e112202, doi: 10.1371/journal.pone.0112202.

Gao, F., J. Masek, M. Schwaller, et al., 2006: On the blending of the Landsat and MODIS surface reflectance: Predicting daily Landsat surface reflectance. *IEEE Trans. Geosci. Remote Sens.*, **44**, 2207–2218, doi: 10.1109/TGRS.2006.872081.

Gao, L., X. F. Wang, B. A. Johnson, et al., 2020: Remote sensing algorithms for estimation of fractional vegetation cover using pure vegetation index values: A review. *ISPRS J. Photogr. Remote Sens.*, **159**, 364–377, doi: 10.1016/j.isprsjprs.2019.11.018.

García-Haro, F. J., F. Camacho de Coca, J. Meliá, et al., 2005: Operational derivation of vegetation products in the framework of the LSA SAF project. Proceedings of EUMETSAT Meteorological Satellite Conference, Dubrovnik, Croatia, 19–23 September, 247–254.

García-Haro, F. J., S. Sommer, and T. Kemper, 2005: A new tool for variable multiple endmember spectral mixture analysis (VMESMA). *Int. J. Remote Sens.*, **26**, 2135–2162, doi: 10.1080/01431160512331337817.

Gong, P., J. Wang, L. Yu, et al., 2013: Finer resolution observation and monitoring of global land cover: First mapping results with Landsat TM and ETM+ data. *Int. J. Remote Sens.*, **34**, 2607–2654, doi: 10.1080/01431161.2012.748992.

Guan, K., E. F. Wood, and K. K. Caylor, 2012: Multi-sensor derivation of regional vegetation fractional cover in Africa. *Remote Sens. Environ.*, **124**, 653–665, doi: 10.1016/j.rse.2012.06.005.

Guerschman, J. P., P. F. Scarth, T. R. McVicar, et al., 2015: Assessing the effects of site heterogeneity and soil properties when unmixing photosynthetic vegetation, non-photosynthetic vegetation and bare soil fractions from Landsat and MODIS data. *Remote Sens. Environ.*, **161**, 12–26, doi: 10.1016/j.rse.2015.01.021.

Gutman, G., and A. Ignatov, 1998: The derivation of the green vegetation fraction from NOAA/AVHRR data for use in numerical weather prediction models. *Int. J. Remote Sens.*, **19**, 1533–1543, doi: 10.1080/014311698215333.

Hu, Z., and D. Zhang, cited. 2006: Country Pasture/Forage Resource Profiles: China. FAO, Rome. [Available online at https://link.springer.com/chapter/10.1007/978-94-024-1617-6_24].

Jarihani, A. A., T. R. McVicar, T. G. Van Niel, et al., 2014: Blending Landsat and MODIS data to generate multispectral indices: A comparison of "Index-then-Blend" and "Blend-then-Index" approaches. *Remote Sens.*, **6**, 9213–9238, doi: 10.3390/rs6109213.

Jia, K., S. L. Liang, S. H. Liu, et al., 2015: Global land surface fractional vegetation cover estimation using general regression neural networks from MODIS surface reflectance. *IEEE Trans. Geosci. Remote Sens.*, **53**, 4787–4796, doi: 10.1109/TGRS.2015.2409563.

Jiapaer, G., X. Chen, and A. M. Bao, 2011: A comparison of methods for estimating fractional vegetation cover in arid regions. *Agric. For. Meteor.*, **151**, 1698–1710, doi: 10.1016/j.agrformet.2011.07.004.

Jiménez-Muñoz, J. C., J. A. Sobrino, A. Plaza, et al., 2009: Comparison between fractional vegetation cover retrievals from vegetation indices and spectral mixture analysis: Case study of PROBA/CHRIS data over an agricultural area. *Sensors*, **9**, 768–793, doi: 10.3390/s90200768.

Lacaze, R., P. Richaume, O. Hautecoeur, et al., 2003: Advanced algorithms of the ADEOS-2/POLDER-2 land surface process line: Application to the ADEOS-1/POLDER-1 data. 2003 IEEE International Geoscience and Remote Sensing Symposium Proceedings, IEEE, Toulouse, France, 3260–3262, doi: 10.1109/IGARSS.2003.1294749.

Li, Q. Z., X. Cao, K. Jia, et al., 2014: Crop type identification by integration of high-spatial resolution multispectral data with features extracted from coarse-resolution time-series vegetation index data. *Int. J. Remote Sens.*, **35**, 6076–6088, doi: 10.1080/01431161.2014.943325.

Liang, S. L., X. Zhao, S. H. Liu, et al., 2013: A long-term Global LAnd Surface Satellite (GLASS) data-set for environmental studies. *Int. J. Digit. Earth*, **6**, 5–33, doi: 10.1080/17538947.2013.805262.

Lobell, D. B., and G. P. Asner, 2002: Moisture effects on soil reflectance. *Soil Sci. Soc. Amer. J.*, **66**, 722–727, doi: 10.2136/sssaj2002.7220.

Lu, H., M. R. Raupach, T. R. McVicar, et al., 2003: Decomposition of vegetation cover into woody and herbaceous components using AVHRR NDVI time series. *Remote Sens. Environ.*, **86**, 1–18, doi: 10.1016/S0034-4257(03)00054-3.

Lucht, W., C. B. Schaaf, and A. H. Strahler, 2000: An algorithm for the retrieval of albedo from space using semiempirical BRDF models. *IEEE Trans. Geosci. Remote Sens.*, **38**, 977–998, doi: 10.1109/36.841980.

Meng, J. H., B. F. Wu, X. Du, et al., 2011: Method to construct high spatial and temporal resolution NDVI DataSet-STAVFM. *J. Remote Sens.*, **15**, 44–59. (in Chinese)

Montandon, L. M., and E. E. Small, 2008: The impact of soil reflectance on the quantification of the green vegetation fraction from NDVI. *Remote Sens. Environ.*, **112**, 1835–1845, doi: 10.1016/j.rse.2007.09.007.

Mu, X. H., S. Huang, H. Z. Ren, et al., 2015: Validating GEOV1 fractional vegetation cover derived from coarse-resolution remote sensing images over croplands. *IEEE J. Sel. Top. Appl. Earth Obs. Remote Sens.*, **8**, 439–446, doi: 10.1109/JSTARS.2014.2342257.

Mu, X. H., W. J. Song, Z. Gao, et al., 2018: Fractional vegetation cover estimation by using multi-angle vegetation index. *Remote Sens. Environ.*, **216**, 44–56, doi: 10.1016/j.rse.2018.06.022.

Naqvi, H. R., J. Mallick, L. M. Devi, et al., 2013: Multi-temporal annual soil loss risk mapping employing Revised Universal Soil Loss Equation (RUSLE) model in Nun Nadi Watershed, Uttrakhand (India). *Arabian J. Geosci.*, **6**, 4045–4056, doi: 10.1007/s12517-012-0661-z.

Obata, K., T. Miura, and H. Yoshioka, 2012: Analysis of the scaling effects in the area-averaged fraction of vegetation cover retrieved using an NDVI-isoline-based linear mixture model. *Remote Sens.*, **4**, 2156–2180, doi: 10.3390/rs4072156.

O'Neill, A. L., 1994: Reflectance spectra of microphytic soil crusts in semi-arid Australia. *Int. J. Remote Sens.*, **15**, 675–681, doi: 10.1080/01431169408954106.

Pan, J. H., and Y. Wen, 2014: Estimation of soil erosion using RUSLE in Caijiamiao watershed, China. *Nat. Hazards*, **71**, 2187–2205, doi: 10.1007/s11069-013-1006-2.

Post, D. F., A. Fimbres, A. D. Matthias, et al., 2000: Predicting soil albedo from soil color and spectral reflectance data. *Soil Sci. Soc. Amer. J.*, **64**, 1027–1034, doi: 10.2136/sssaj2000.6431027x.

Price, J. C., 1992: Estimating vegetation amount from visible and near infrared reflectances. *Remote Sens. Environ.*, **41**, 29–34, doi: 10.1016/0034-4257(92)90058-R.

Purevdorj, T., R. Tateishi, T. Ishiyama, et al., 1998: Relationships between percent vegetation cover and vegetation indices. *Int. J. Remote Sens.*, **19**, 3519–3535, doi: 10.1080/014311698213795.

Roujean, J.-L., and R. Lacaze, 2002: Global mapping of vegetation parameters from POLDER multiangular measurements for studies of surface-atmosphere interactions: A pragmatic method and its validation. *J. Geophys. Res. Atmos.*, **107**, 4150, doi: 10.1029/2001JD000751.

Roy, D. P., J. C. Ju, P. Lewis, et al., 2008: Multi-temporal MODIS–Landsat data fusion for relative radiometric normalization, gap filling, and prediction of Landsat data. *Remote Sens. Environ.*, **112**, 3112–3130, doi: 10.1016/j.rse.2008.03.009.

Sexton, J. O., X.-P. Song, M. Feng, et al., 2013: Global, 30-m resolution continuous fields of tree cover: Landsat-based rescaling of MODIS vegetation continuous fields with lidar-based estimates of error. *Int. J. Digit. Earth*, **6**, 427–448, doi: 10.1080/17538947.2013.786146.

Singh, R. P., S. Goroshi, N. K. Sharma, et al., 2011: Remote sensing based biophysical characterization of tropical deciduous forest in central India. ISPRS Bhopal 2011 Workshop, Bhopal, India, XXXVIII-8/W20, 145–149, doi: 10.5194/isprsarchives-XXXVIII-8-W20-145-2011.

Song, W. J., X. H. Mu, G. Y. Ruan, et al., 2017: Estimating fractional vegetation cover and the vegetation index of bare soil and highly dense vegetation with a physically based method. *Int. J. Appl. Earth Obs. Geoinf.*, **58**, 168–176, doi: 10.1016/j.jag.2017.01.015.

Verger, A., F. Baret, and M. Weiss, 2014: Near real-time vegetation monitoring at global scale. *IEEE J. Sel. Top. Appl. Earth Obs. Remote Sens.*, **7**, 3473–3481, doi: 10.1109/JSTARS.2014.2328632.

Verger, A., F. Baret, M. Weiss, et al., 2015: GEOCLIM: A global climatology of LAI, FAPAR, and FCOVER from VEGETATION observations for 1999–2010. *Remote Sens. Environ.*, **166**, 126–137, doi: 10.1016/j.rse.2015.05.027.

Walker, J. J., K. M. de Beurs, and R. H. Wynne, 2014: Dryland vegetation phenology across an elevation gradient in Arizona, USA, investigated with fused MODIS and Landsat data. *Remote Sens. Environ.*, **144**, 85–97, doi: 10.1016/j.rse.2014.01.007.

Wang, J. A., and W. Zuo, 2010: *Geographic Atlas of China.* SinoMaps Press, Beijing, 362 pp.

Weiss, D. J., P. M. Atkinson, S. Bhatt, et al., 2014: An effective approach for gap-filling continental scale remotely sensed time-series. *ISPRS J. Photogr. Remote Sens.*, **98**, 106–118, doi: 10.1016/j.isprsjprs.2014.10.001.

Weiss, M., F. Baret, S. Garrigues, et al., 2007: LAI and fAPAR CYCLOPES global products derived from VEGETATION. Part 2: Validation and comparison with MODIS collection 4 products. *Remote Sens. Environ.*, **110**, 317–331, doi: 10.1016/j.rse.2007.03.001.

Wilson, A. M., and W. Jetz, 2016: Remotely sensed high-resolution global cloud dynamics for predicting ecosystem and biodiversity distributions. *PLoS Biol.*, **14**, e1002415, doi: 10.1371/journal.pbio.1002415.

Wu, D. H., H. Wu, X. Zhao, et al., 2014: Evaluation of spatiotemporal variations of global fractional vegetation cover based on GIMMS NDVI data from 1982 to 2011. *Remote Sens.*, **6**, 4217–4239, doi: 10.3390/rs6054217.

Xiao, J. F., and A. Moody, 2005: A comparison of methods for estimating fractional green vegetation cover within a desert-to-upland transition zone in central New Mexico, USA. *Remote Sens. Environ.*, **98**, 237–250, doi: 10.1016/j.rse.2005.07.011.

Xie, Y. Y., and A. M. Wilson, 2020: Change point estimation of deciduous forest land surface phenology. *Remote Sens. Environ.*, **240**, 111698, doi: 10.1016/j.rse.2020.111698.

Yan, G., X. Mu, and Y. Liu, 2012: Fractional vegetation cover. *Advanced Remote Sensing*, Liang, S. L., X. W. Li, and J. D. Wang, Eds., Academic Press, Amsterdam, 415–438.

Yang, L. Q., K. Jia, S. L. Liang, et al., 2017: A robust algorithm for estimating surface fractional vegetation cover from Landsat data. *Remote Sens.*, **9**, 857, doi: 10.3390/rs9080857.

Zeng, X. B., R. E. Dickinson, A. Walker, et al., 2000: Derivation and evaluation of global 1-km fractional vegetation cover data for land modeling. *J. Appl. Meteor.*, **39**, 826–839, doi: 10.1175/1520-0450(2000)039<0826:DAEOGK>2.0.CO;2.

Zhang, X., G. Yan, Q. Li, et al., 2006: Evaluating the fraction of vegetation cover based on NDVI spatial scale correction model. *Int. J. Remote Sens.*, **27**, 5359–5372, doi: 10.1080/01431160600658107.

Zhang, X. P., D. L. Pan, J. Y. Chen, et al., 2013: Using long time series of Landsat data to monitor impervious surface dynamics: A case study in the Zhoushan Islands. *J. Appl. Remote Sens.*, **7**, 073515, doi: 10.1117/1.jrs.7.073515.

Zhang, X. S., 1993: A vegetation-climate classification system for global change studies in China. *Quat. Sci.*, **13**, 157–169. (in Chinese)

Zhang, X. W., and B. F. Wu, 2015: A temporal transformation method of fractional vegetation cover derived from high and moderate resolution remote sensing data. *Acta Ecol. Sinica*, **35**, 1155–1164, doi: 10.5846/stxb201305020904. (in Chinese)

Zhang, Y. S., A. Harris, and H. Balzter, 2015: Characterizing fractional vegetation cover and land surface temperature based on sub-pixel fractional impervious surfaces from Landsat TM/ETM+. *Int. J. Remote Sens.*, **36**, 4213–4232, doi: 10.1080/

01431161.2015.1079344.

Zhang, Z. X., X. Wang, X. L. Zhao, et al., 2014: A 2010 update of National Land Use/Cover Database of China at 1:100000 scale using medium spatial resolution satellite images. *Remote Sens. Environ.*, **149**, 142–154, doi: 10.1016/j.rse.2014.04.004.

Zhu, X. L., J. Chen, F. Gao, et al., 2010: An enhanced spatial and temporal adaptive reflectance fusion model for complex heterogeneous regions. *Remote Sens. Environ.*, **114**, 2610–2623, doi: 10.1016/j.rse.2010.05.032.

Tech & Copy Editor: Qi WANG